Ultra relativistic Weibel-like instabilities investigated with a Semi-Lagrangian adaptive mesh refinement method

M. Antoine[1], A. Ghizzo[1], E. Deriaz[2], D. Del Sarto[1]

[1] *Institut Jean Lamour, CNRS - Université de Lorraine, Nancy 54000, France.* [2] *International Innovation Institute, Beihang University, 311115 Hangzhou, China.*

Semi-Lagrangian codes are often used to solve the evolution of the distribution function for a collisionless plasma. However, they generally require large computational resources, especially to describe the filamentation, which is a key element of the energy transfer towards microscopic scales and which intervenes in a variety of plasma processes like Weibel-type instabilities [1] or magnetic reconnection [2, 3] (which are relevant to a variety of phenomena, e.g., gamma-ray bursts, interpenetrating flows, laser plasma interactions, etc...). An integration strategy using an embedded grid refinement only in momentum space helps to overcome this issue. We have implemented it in the semi-lagrangian VLEM code [4] and we have applied it to an ultrarelativitic case.

Weibel-type instabilities can be divided into three categories of electron-beam-plasma instability: the current filamentation instability (CFI) [5, 6], driven by a momentum anisotropy (with the wavevector $\mathbf{k}$, being perpendicular to the beams), the electrostatic two-stream instability (TSI), with $\mathbf{k}$ aligned to the beams, and finally the oblique instability (OI) [7, 8], for an arbitrary direction of $\mathbf{k}$.

We will investigate these instabilities in the context of an ultrarelativistic system consisting of two counter-streaming electron beams. To do so, we will use the Maxwell–Jüttner distribution function [9], which in two dimensions of space and two dimensions of momentum, is written as follows for the electron beam j:

$$F_{0j} = A\exp\left(-\theta_j^{-1}(\gamma(\mathbf{p}) - \beta_j p_y)\right), \tag{1}$$

with A the normalisation factor, β_j the normalised drift velocity in y direction, $\gamma(\mathbf{p})$ the relativistic factor and $1/\theta_j = mc^2/(k_B T_j)$.

We will consider the case of a cold beam and a hot beam propagating in opposite directions along the y-axis. For the cold beam we choose a temperature $k_B T_1 = 5keV$ and for the relativistic hot beam we choose $k_B T_2 = 2000keV$, with an equivalent density between the two beams ($n_1 = n_2 = n_0/2$) and $\beta_1 = -\beta_2 = -0.745$. Those parameters correspond to the results from Bret et al. [7] , which we have adapted to our case in figure 1 (left).

The system is perturbed to either excite only the OI (green triangle in figure 1 (left)) or

the OI, CFI and TSI (white circles in figure 1 (left)). To do this, we choose $L_x = 15.707 d_e$ and $L_y = 20.943 d_e$ for the normalised size of the box, which corresponds to $\Delta k_x d_e = 0.40$ and $\Delta k_y d_e = 0.30$. The initial perturbation is applied to the B_z component in the form:

$$\delta B_z = \delta B_0 \left[\sum_{(n_x, n_y)} \sin(n_x \Delta k_x x + n_y \Delta k_y y) \right], \tag{2}$$

with $e \delta B_0 / (m \omega_p) = 0.005$ and $(n_x, n_y) = (1,1)$ for the excitation of the OI and $(n_x, n_y) = (1,1)$, $(1,0)$ and $(0,1)$ for the multiple mode excitation. We choose $\Delta t \omega_p = 0.01$ and take 36 000 time steps. For the spatial grid, we have $N_x N_y = 256^2$ over 2048 processors (256 MPI processes with 8 OpenMP tasks). We choose $\varepsilon = 10^{-7}$ for the refinement criterion [4], with a maximum number of points for the grid $R = R^{max} = 3$ equal to $N_{p_x} = 505$ and $N_{p_y} = 1017$ with the box limit of the momentum space $p_{x_{min}} / p_{x_{max}} = -40mc/40mc$ and $p_{y_{min}} / p_{y_{max}} = -20mc/100mc$.
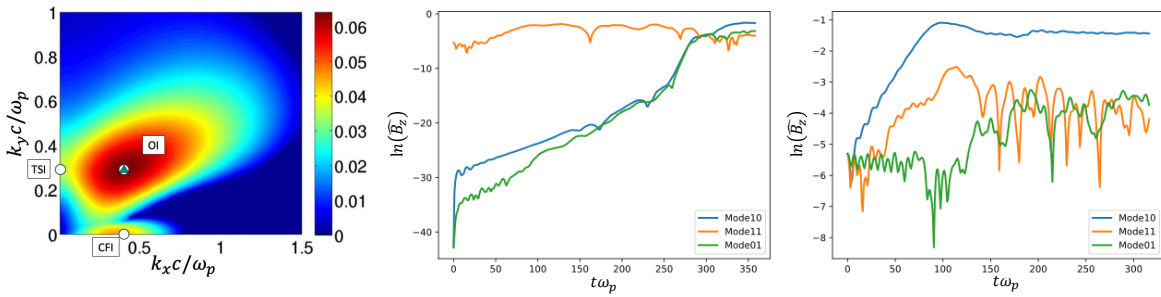

Figure 1: (Left) Maximum growth rate representation for the chosen parameters. This figure has been slightly modified from Bret et al. [7]. The evolution of the magnetic component, $\hat{B}_z(n_x \Delta k_x, n_y \Delta k_y)$ is shown for $(n_x, n_y) = (1,0)$, $(1,1)$ and $(0,1)$ which correspond respectively to CFI, OI and TSI. The initial perturbation is on either the mode $(1,1)$ (middle) or on the three modes $(1,0)$, $(1,1)$ and $(0,1)$ (right).

Figure 1 (middle) shows the evolution of the magnetic field component $\hat{B}_z$ for the case where only the OI is excited. From this figure, we can extract the numerical growth rate, denoted by $\Gamma_{n_x n_y}^{num}$. It can be seen that the OI starts at a higher level, whereas the other modes start at the machine error. The growth rate for the $\Gamma_{11}^{num} / \omega_p = 0.060$ which is quite close to the theoretical growth rate $\Gamma_{11}^{th} / \omega_p = 0.065$ (see figure 1 left). However, for the CFI, we observe a growth rate of $\Gamma_{10}^{num} / \omega_p = 0.055$ between $t \omega_p \simeq 0$ and 150, then $\Gamma_{10}^{num} / \omega_p = 0.078$ between $t \omega_p \simeq 150$ and 250 and $\Gamma_{10}^{num} / \omega_p = 0.299$ between $t \omega_p \simeq 250$ and 280. All these growth rates are higher than the theoretical value $\Gamma_{10}^{th} / \omega_p = 0.045$, but the one between $t \omega_p \simeq 0$ and 150, which is therefore the least impacted by the non-linear effects of OI, is lower than $\Gamma_{11}^{num} / \omega_p$, which is coherent

with the theoretical results (figure 1 left). We also observe a transition from OI to CFI in the non-linear phase.

The existence of three different growth rates, as well as the transition from OI to CFI, raises questions about the role of non-linear effects due to OI. To address this, we will excite the three instabilities (OI, CFI and TSI) in order to compare the growth rates in the absence of non-linear effects. The growth rates when these three instabilities are extracted from the figure 1 (right). We now find a growth rate of $\Gamma_{10}^{num}/\omega_p = 0.048$ for the CFI, which is fairly close to the theoretical rate. However, for the OI, the growth rate $\Gamma_{11}^{num}/\omega_p = 0.035$ is lower than the theoretical rate but also lower than that of the CFI. The CFI instability is also the one that saturates with a higher intensity. We can therefore deduce that, experimentally, CFI is the most unstable for these parameters.
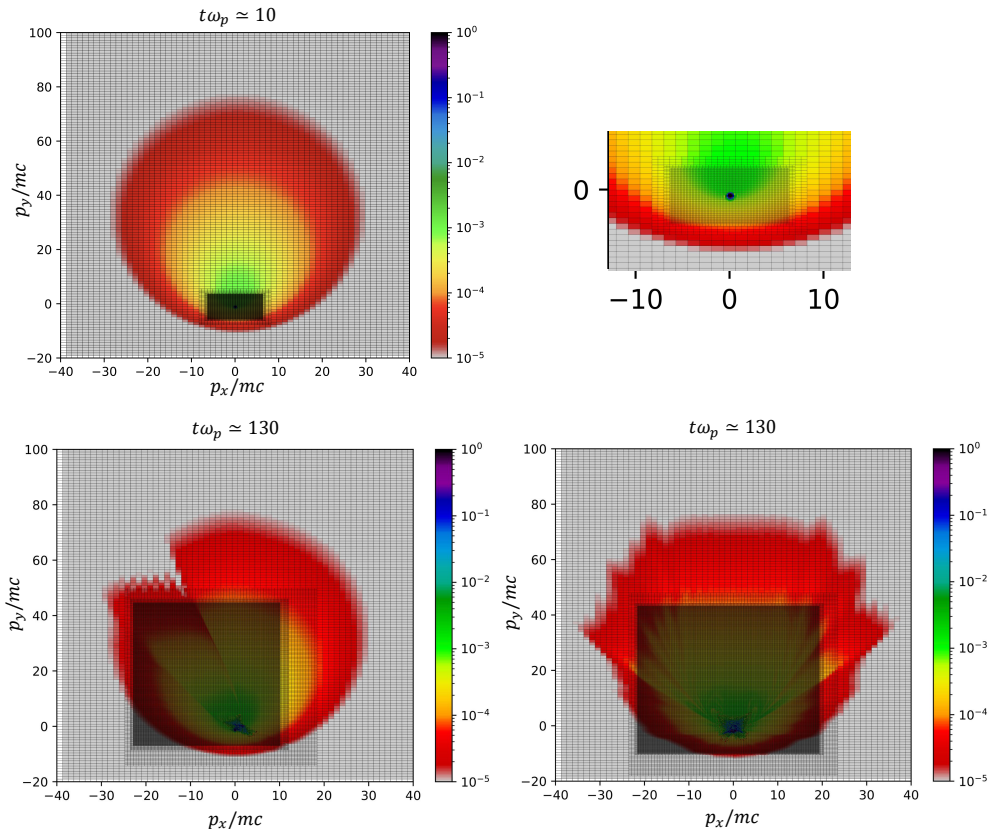

Figure 2: Representation of the distribution function in $p_x - p_y$ phase space for a point located at $(i_x = N_x/2, i_y = N_y/2)$. At the initial time $t\omega_p \simeq 0$, the distribution function is the same for both excitations, and is represented with embedded grids (top-left) and a grid zoom ($R = R^{max} = 3$) (top-right). The distribution function is shown at $t\omega_p \simeq 130$ for initial excitations on either the OI (bottom-left) or multiple modes (bottom-right). The embedded grids accurately follow the evolution of the distribution function.

On the other hand, we can see from figure 2 that the VLEM_EG code [4] is well adapted

to this kind of simulation. Initially, the distribution function looks the same for both cases, and the grid has refined only the distribution of the cold beam (top-right). With the old version of the code, the grid would take up the entire phase space with high precision, which would increase the computational time. We also note that, at time $t\omega_p \simeq 130$, the filamentation of the distribution function is well followed by the grids. For the case where we first excite OI, there is an asymmetry representative of this instability (bottom-left). In contrast, for multiple mode excitation, we observe a symmetric evolution of the distribution function, representative of the CFI (bottom-right).

To conclude, embedded grids are well adapted to relativistic distributions, even when there is a significant temperature difference between two beams. This makes it possible to perform simulations that where never done before with a Semi-Lagrangian method. The results presented suggested the CFI to be the most unstable mode, differently from what indicated by previous theoretical predictions [7]. Further work is needed to understand the reasons why.

This method can be used even to study Weibel instabilities initialized without perturbations, i.e., with perturbations having a machine error amplitude - a kind of problem for which non-PIC codes are well adapted due to their initial "noiseless" character.

References

[1]   A. Ghizzo et al., *Phys. Rev. Lett.* (**131**), p. 035101. (2023).

[2]   H. Wiechen, *Annales Geophysicae* (**17**), pp. 595–603. (1999).

[3]   H. J. Ziegler et al., *Monthly Notices of the Royal Astronomical Society* (**232**), pp. 623–646. (1998).

[4]   M. Antoine et al., *Physics of Plasmas* (**32**), p. 043905. (2025).

[5]   B. D. Fried, *Phys. Fluids* (**2**), p. 337. (1959).

[6]   G. Raj et al., *American Physical Society* (**2**), p. 023123. (2020).

[7]   A. Bret et al., *Physical Review E* (**81**), p. 036402. (2010).

[8]   L. Gremillet et al., *Phys. Plasmas* (**14**), p. 040704. (2007).

[9]   F. Jüttner, *Annalen der Physik* (**339**), pp. 856–882. (1911).